Applied Catalysis B: Environmental 325 (2023) 122317

Contents lists available at ScienceDirect

Applied Catalysis B: Environmental

journal homepage: www.elsevier.com/locate/apcatb

P-induced Co-based interfacial catalysis on Ni foam for hydrogen generation from ammonia borane

Sehrish Mehdi [a], Yanyan Liu [a,b,*], Huijuan Wei [a], Huanhuan Zhang [a], Ruofan Shen [a], Shuyan Guan [a], Xianli Wu [a], Tao Liu [c], Hao Wen [a], Zhikun Peng [a], Chengming Wang [a,**], Zhongyi Liu [a], Huaqiang Cao [d], Baojun Li [a,**]

[a] Research Center of Green Catalysis, College of Chemistry, Zhengzhou University, 100 Science Road, Zhengzhou 450001, PR China
[b] College of Science, Henan Agricultural University, Zhengzhou, Henan 450002, PR China
[c] CAS Key Laboratory for Biomedical Effects of Nanomaterials and Nanosafety, National Center for Nanoscience and Technology, Beijing 100190, PR China
[d] Department of Chemistry, Tsinghua University, Beijing 100084, PR China

ARTICLE INFO

Keywords:
Co-CoP interfaces
Monolith
Manual coating
Nickel foam
Ammonia borane hydrolysis

ABSTRACT

Co-based monolithic phosphides have caught attention due to their stability and corrosion resistance properties during the catalytic reaction. Herein, P-induced Co-based interfacial phosphides Co-CoP-NC/NF are prepared through the PH_3-phosphorization. The theoretical and experimental analysis confirms the uniform growth of Co-CoP nanoparticles (NPs) with turmeric-like morphology. Co-CoP NPs (average size = 8.78 nm) express prominent interfacial interaction and a strong electronic interaction between metal sites and doped phosphorous (P). Thus, P inducing synergistically increases the number of catalytic active sites (CoP) and electronic modulation of metallic sites (Co). The optimized catalyst Co-CoP-NC/NF-2 express the excellent and the best-ranked catalytic activity for ammonia borane hydrolysis with hydrogen evolution rate (r_B = 2500 mL min^{-1} g_{Co}^{-1}), turnover frequency ($TOF = 600\ h^{-1}$), and apparent activation energy (E_a = 30.6 kJ mol^{-1}). This work provides a potential avenue for developing monolithic catalysts for industrial applications in the field of heterogeneous catalysis and sustainable energy.

1. Introduction

In the current era, with the increase of industrialization, the risk of depletion of energy sources has increased. There is a dire need for the replacement of fossil fuels as a future energy source [1]. Hydrogen has appeared as a potential candidate due to its clean and renewable energy characteristics [2,3]. In the last decades, boron hydrides have been studied extensively as secure and efficient hydrogen storage materials [4–6]. Among boron hydrides, ammonia borane (NH_3BH_3, AB) has occupied a distinct position due to its stability, high hydrogen content (19.6 wt%), non-toxicity, and eco-friendly nature [7]. Despite these facts, due to slow reaction kinetics, a suitable catalyst is required for the controlled and efficient hydrogen evolution from NH_3BH_3 on hydrolysis under ambient conditions (Eq. (1)) [8].

$$NH_3BH_3 + 2H_2O \rightarrow NH_4^+ + BO_2^- + 3H_2\uparrow \quad (1)$$

Noble metal (Pt [9,10], Pd [1], Ru [11]) catalysts have been studied extensively for ammonia borane hydrolysis with outstanding catalytic activity [12]. The scarcity and high cost of noble metals are limiting factors in the field of catalysis [13]. In this perspective, the use of alternative economic metals (Co [14], Fe, Ni [15], Cu [16]) is an attractive approach [17,18]. However, the mono-metallic catalyst still suffers from lower catalytic activity due to aggregation and low dispersion of metal active sites. The introduction of new catalytic active sites via doping of heteroatom (S, N, P) is an attractive strategy to enhance the activity, selectivity, and stability of a non-noble catalyst [19–21].

Monolithic catalysts have caught attention due to their facile preparation and use for catalytic reactions [22–24]. From the operational point of view, it is advantageous to use a monolithic catalyst to adjust the surface morphology and structure [25]. Further, the facile separation from the reaction mixture after the catalytic reaction is an economic

* Corresponding author at: Research Center of Green Catalysis, College of Chemistry, Zhengzhou University, 100 Science Road, Zhengzhou 450001, PR China.
** Corresponding authors.
E-mail addresses: lyycarbon@henau.edu.cn (Y. Liu), hitwcm@zzu.edu.cn (C. Wang), lbjfcl@zzu.edu.cn (B. Li).

https://doi.org/10.1016/j.apcatb.2022.122317
Received 28 August 2022; Received in revised form 13 December 2022; Accepted 19 December 2022
Available online 20 December 2022

factor for monolithic catalysts [26]. However, the selection of suitable support, metal, and support-metal interaction has an important role in the preparation of an efficient monolithic catalyst. The suitable loading and uniform dispersion of active sites are prime factors for increasing the efficiency of a catalyst [27]. Ni foam, Fe foam, and carbon cloth have been studied extensively in this regard [2,28]. However, the self-aggregation, instability, poor dispersion, and insufficient interaction of active sites with the support cause a decrease in the catalytic activity of monolithic catalysts during the catalytic process. To address this problem, the doping of a metal specie with an electronegative element has become an attractive tactic to increase the number and modulate the electronic surrounding of metal active sites in a catalyst [29]. Various transition metal-based oxides [8], phosphides [14,20], and nitrides [30] have been studied in this context. Among all these catalysts, the transition metal phosphides are widely reported as an efficient catalyst for ammonia borane hydrolysis with the appropriate charge transfer from metal to phosphorous (P) [13,31,32]. The inducing of phosphorous elements to the metallic center creates unbalanced charge distribution due to differences in electronegativity of partial negative (P) and partial positive metallic center (M) [33,34]. The adherence of phosphorous (P) to a monolithic catalyst is promising for modifying the electronic structure by regulating the density of D-states around the fermi level of metallic active centers [35]. The regulation of active sites in the phosphorous framework and enhanced surface area of support increases the electronic interaction across the active metal sites and support during the catalytic process [21,36]. For, example, Wang's group has prepared well-dispersed Co@Co_2P core-shell nanoparticles embedded in N-doped carbon nanotube polyhedrons via carbonization and phosphidation of ZIF-67 [35]. Kwang Sup Eom et al reported electroplated Co-P on a commercial nodule Cu sheet with amorphous Co-P and Co nanoparticles [37]. Liang Cui et al introduced the CoP nanowires array prepared on a Ti mesh (CoP NA/Ti) monolithic catalyst using on/off switch demand for hydrogen generation [38]. Beyza Nur Kinsiz et al reported a Co_3O_4 beads-like catalyst prepared from a Co-alginate capsule using a nano-casting procedure expressing the easily separated reaction mixture [39]. Jingang Yang et al prepared quaternary cobalt-tungsten-boron-phosphorous porous particles supported on the Ni foam surface (Co-W-B-P/Ni) through ultrasonification-assisted electroless deposition route for the NH_3BH_3 hydrolysis [40]. Similarly, many other research groups have discussed the advantage of monolithic catalysts over powder catalysts for hydrogen generation from ammonia borane [27,29]. However, for monolithic catalysts, the complex reaction strategies and use of binders still compromise the competitiveness of non-noble metal phosphides [41]. Thus, a simple, binder-free, and facile strategy needs attention to develop competitive transition metal phosphides in the field of catalysis.

In this work, the preparation of P-induced Co-based monolithic catalysts via a facile and economic synthesis strategy is addressed. Further, the introduction of P precursor for improving the number and electronic modulation of active sites in the prepared catalysts is focused on. The existence of Co-CoP interfaces embedded into the carbon-nitrogen (CN) matrix promotes new active sites for the efficient adsorption of reactants molecules due to electron transfer from Co to P [13]. Thus, the inducing of P improves the catalytic activity of prepared monolithic catalysts. In addition, Zeolitic imidazole framework-67 (ZIF-67) has been used as a favorable precursor for the preparation of a Co-based catalyst. The sufficient N content and porosity provide stable and high electronic conductivity to Co active sites in the N-doped mesoporous graphitic carbon. Briefly, the previously reported strategy is adopted to achieve Co-NC/NF with some modifications [27]. Then, the P-induced Co-CoP interfaces embedded in the carbon-nitrogen matrix (CN) are received via PH_3-phosphorization. The optimized catalyst Co-CoP-NC/NF-2 with dispersed Co and CoP active sites is studied for NH_3BH_3 hydrolysis in alkaline-free reaction conditions. The synergistic effect of Co-CoP interfaces provides scalable stability, cyclability, and improved catalytic activity for the hydrolysis of NH_3BH_3 through the water displacement method. Importantly, the prepared robust Co-CoP-NC/NF-2 interfacial catalyst reveals remarkable efficient hydrogen (H_2) evolution from NH_3BH_3 in comparison to previous monolithic catalysts presented in the literature. The designed monolithic catalyst directs a new route for the development of potential monolithic catalysts in the field of sustainable energy and heterogeneous catalysis.

2. Experimental section

2.1. Preparation of catalysts

2.1.1. Two-step preparation of ZIF-67/NF precursor (ZIF preparation)

Firstly, zeolite imidazole framework-67 (ZIF-67) powder was prepared by the previously reported method with some modifications [42,43]. 2-methylimidazole (1.641 g) was dissolved in methanol (30 mL) to form a clear solution and poured dropwise into methanol solution (30 mL) of $Co(NO_3)_2{\cdot}6\ H_2O$ (2.91 g) under stirring (300 rpm, 30 min). The purple ZIF-67 precipitates appeared during stirring. Further, the reaction mixture was aged overnight at room temperature. The aged ZIF-67 was collected after centrifugation (6000 rpm, 5 min) and washed with anhydrous methanol three times. Afterward, ZIF-67 was dried in a pre-heated electric oven (60 °C, 10 h), and ground in a mortar (10 min) to receive its fine powder (0.1 g).

2.1.2. Preparation of ZIF-67/NF precursor by ex-situ coating and pressing method

ZIF-67/NF precursor was prepared according to the previous report with some modifications [27]. Nickel foam (2 cm × 2 cm × 1.5 mm, 0.15 g) was pretreated with 1 M HCl solution for 30 min to clean surface oxides. Further, Ni foam was washed with deionized water and anhydrous methanol thoroughly. After overnight drying at 30 °C in a pre-heated electric oven, Ni foam was used as the substrate for the next step. ZIF-67 powder (0.05 g) was sprinkled uniformly with a spatula on both sides of the nickel foam. Ni foam with sprinkled ZIF-67 powder was pressed mechanically with a tableting machine at up to 1 MPa pressure. The resulting precursor ZIF-67/NF (0.197 g ± 0.002 g) was used directly for the next step. The r_B and *TOF* were calculated concerning the actual loaded amount of ZIF-67 in the ZIF-67/NF precursor (0.047 g ± 0.002 g).

2.1.3. Preparation of Co-NC/NF

The prepared ZIF-67/NF (0.197 g) precursor was placed in a porcelain boat and pyrolyzed at 600 °C for 30 min with a ramped rate of 10 °C per minute under Ar gas followed by cooling at room temperature to obtain Co-NC/NF. Co-NC/NF was received from the tube furnace after passivation with ethanol to avoid air-exposed oxidation. The passivated catalyst was dried at 60 °C for 2 h in a pre-heated electric oven.

2.1.4. Preparation of Co-CoP-NC/NF

Co-NC/NF (0.172 g), and $NaH_2PO_2{\cdot}H_2O$ with a weight ratio (1:10) were placed in two different porcelain boats at a distance of 2 cm in a tube furnace. $NaH_2PO_2{\cdot}H_2O$ was used as a phosphorous (P) source and placed in a porcelain boat upstream of the tube furnace. Co-NC/NF was placed downstream of the tube furnace. The phosphorization process was carried out at 300 °C for 30, 60, and 120 min with a ramped rate of 5 °C per minute under Ar gas. The catalyst Co-CoP-NC/NF was received after natural cooling of the tube furnace up to room temperature. The optimized monolithic catalyst Co-CoP-NC/NF-2 (0.186 g) with phosphorization (1:10, 60 min) was considered for next all experiments in this work. The detail of optimization reactions is provided in the supplementary information.

2.2. Ammonia borane hydrolysis in the batch reactor

The hydrolysis of NH_3BH_3 was studied through water displacement with some modifications to the previously reported method [15].

Co-CoP-NC/NF-2 (2 cm × 2 cm × 1.5 mm, 0.186 g) was placed in the round bottom flask (50 mL) fixed on an electric heated thermostatic water bath (303 K, 500 rpm). NH_3BH_3 (72 mg) in deionized water (15 mL, 155 mM) was stirred (300 rpm, 10 min). The clear solution of NH_3BH_3 (155 mM) was quickly poured into an already fixed round bottom flask. A water-filled beaker (250 mL) situated in a water-filled vessel was used to record the volume of H_2 through water displacement. An efficient H_2 evolution was observed on the surface of the catalyst after the injection of the NH_3BH_3 solution. The hydrogen evolution specific rate (r_B) was calculated by using H_2 evolution recorded data according to the following formula (Eq. (2)) [44,45].

$$r_B = \frac{60(mL)}{[t_{90-}t_{30}](\text{min}) \times w_c(g)} \quad (2)$$

where, r_B = specific rate of hydrogen evolution (mL g^{-1} min^{-1}), t_{90} = time (min) for 90 mL of hydrogen evolution, t_{30} = time (min) for 30 mL of hydrogen evolution, w_c = weight (g) of active metal (Co) loaded on the Ni foam.

The value of *TOF* was calculated by the following formula (Eq. (3)):

$$TOF = \frac{n_{H2}}{n_{Co} \times t(\text{min})} \quad (3)$$

where n_{H2} is the mole of H_2 generated during 30–90 mL, n_{Co} is the mole of Co in the catalyst, and t is the reaction time (t_{90}-t_{30}) (min).

The monolithic Co-CoP-NC/NF-2 was collected from the reaction mixture after NH_3BH_3 hydrolysis. The used Co-CoP-NC/NF-2 was washed three times with water and ethanol. The used catalyst was dried at 30 °C overnight, weighed, and used for next use.

The reusability test was performed in a batch reactor for five cycles. The catalyst was heated (200 °C, 2 h) in the air before every next reuse.

2.3. Material characterization

Powder X-ray diffraction (PXRD) studies of catalyst were performed on Bruker D8 Advance X-ray diffractometer with Cu-Kα (λ = 1.5418 Å) with a diffraction angle of 5–81° (2θ) at a rate of 10° min^{-1}. The microstructure of the synthesized catalyst was studied on an emission scanning electron microscope (SEM, ZEISS Sigma 500), and transmission electron microscope (TEM, FEI Tecnai G^2 F20 S-TWIN electron microscope operated at 200 kV). X-ray Photoelectron spectra (XPS) were conducted on a PHI quantera SXM spectrometer (Al excitation source, Kα = 1486.6 eV), and binding energies were calibrated by referencing C 1 s peak (284.8 eV). PXRD, XPS, and TEM analysis was performed by scratching powder catalyst from the surface of nickel foam while the whole catalyst, Co-CoP-NC/NF (2 cm × 2 cm × 1.5 mm) was used for SEM and ammonia borane hydrolysis studies for this work.

2.4. DFT simulations

The first-principles calculations of the Vienna Ab-initio Simulation Package (VASP) were used to investigate the Co-CoP-NC structures based on DFT. For more experimental details, see the supporting information.

3. Results and discussion

3.1. Fabrication, morphology, and elemental composition

Zeolite imidazole framework-67 (ZIF-67) is used as a source of Co to prepare a Co-based monometallic monolithic catalyst, Co-CoP-NC/NF, for NH_3BH_3 hydrolysis. The promising adhesion fabrication compatibility of ZIF-67 powder with the porous nickel foam assists in the uniform dispersion of active material on the support. Firstly, Co-NC/NF is received via a previously reported manual-coated ZIF-67/NF precursor strategy with some modifications [27]. In the PH_3-phosphorization process, $NaH_2PO_2{\cdot}H_2O$ is used as the source of phosphorous (P) precursor. $NaH_2PO_2{\cdot}H_2O$ dissociates to PH_3 gas after heating and the surface of Co-NC/NF is phosphorized as Co-CoP-NC/NF interfacial catalyst (Fig. 1). The PH_3-phosphorization process is based on the process ($2NaH_2PO_2{\cdot}H_2O \rightarrow PH_3 + Na_2HPO_4 + 2\,H_2O$) [46]. The extent of P precursor is studied at different amounts of $NaH_2PO_2{\cdot}H_2O$ concerning the weight ratio of Co-NC/NF. To achieve optimum catalyst, some preliminary experiments are performed. A volcano trend is observed from low (1:1) to high amounts (1:20) of $NaH_2PO_2{\cdot}H_2O$ (Fig. S1). Further, some contrast reactions are performed to receive the eco-friendly and mild reaction conditions (Fig. S2). The phosphorization time (30, 60, 120 min) is studied to obtain the best-optimized catalyst (Fig. S3). Thus, the adopted reaction conditions are properly optimized and suitable reaction conditions are adopted to receive robust structural and catalytic properties of optimized catalyst Co-CoP-NC/NF-2 (1:10, 60 min). The fabricated amount of Co-CoP-NC on the nickel foam is calculated as 0.036 g. The increase in weight of Co-CoP-NC/NF-2 (0.014 g) after PH_3-phosphorization indicates the successful P-inducing into the Co-NC/NF. Further, the profile of all catalysts (Table S1), necessary mathematical expressions (Eq. (S1)), and experimental details of comparison reactions are listed in the supporting information.

PXRD studies show strong and characteristic peaks at 7.356° (011), 12.737° (112), and 18.051° (222) for as-prepared ZIF-67 [47] (Fig. S4a). Thus, the ZIF-67 expresses high crystallinity through the adopted protocol. The PXRD pattern of Ni foam expresses the prominent characteristic peaks and structural stability under the adopted reaction conditions [27] (Fig. S4b). The PXRD pattern of Co-NC/NF shows the characteristic peaks of nanocrystalline cubic Co^0 phases at 44.2° (111), 51.5° (202), and 75.8° (220) (JCDPS No. 15–0806). The wide diffraction peak of graphitic carbon appears from 14.8° to 34.2° [48] (JCDPS No. 50–0926) (Fig. 2a). The PXRD pattern of Co-CoP-NC/NF-2 shows the diffraction peaks of CoP (JCPDS No. 29–0497). The diffraction peaks at 36.3° (111), 46.2° (112), 48.1° (211), 52.2° (103), and 56.7° (301) show the existence of orthorhombic CoP phases [20,49]. The less obvious peaks of CoP phases express the homogeneous distribution of CoP phases throughout the catalyst. In addition, less prominent CoP peaks in the PXRD pattern occur possibly due to the nanocrystal structure and low loading amount of the catalyst. The existence of cubic Co^0 phases at 44.2° (111), and 51.5° (202) in Co-CoP-NC/NF-2 express the partial phosphorization of Co species during the PH_3-phosphorization process. Thus, the obvious change in the PXRD pattern of Co-NC/NF to Co-CoP-NC/NF-2 exhibits the successful inducing of P species in the as-prepared catalyst. Further, the less prominent Co peak at 60 min of PH_3-phosphorization shows the optimum P-inducing in the Co-CoP-NC/NF-2 catalyst due to the effect of the extent of P precursor on phases and internal structure of the Co species [21] (Fig. S5a).

The scanning electron microscope (SEM) images express the successful growth of Co-CoP NPs on the surface of Ni foam. Co-CoP NPs show the turmeric-like morphology uniformly fabricated on Ni foam (Fig. 2b and inset Fig. 2c). The EDS-SEM elemental mapping confirms the existence of Co, P, O, C, and N elements in the carbon-nitrogen matrix (Fig. 2d). The porous and rough morphology may be attributed to the PH_3 gas interaction with Co-NC/NF during PH_3-phosphorization [48]. Thus, the Co-CoP-NC/NF-2 interface catalyst expresses a large surface area, suitable for the catalytic reaction with exposed active sites. TEM images reveal the formation of Co-CoP NPs encapsulated by a carbon-nitrogen matrix (Fig. 3a, b). The mean size of Co-CoP nanoparticles appears to be 8.78 nm (inset of Fig. 3a). The energy dispersive spectrum (EDX) confirms the existence of Co, P, O, N, and C elements (inset of Fig. 3b). The interfacial interaction of Co and CoP NPs is prominent in the catalyst (Fig. 3c). The high-resolution (HRTEM) images exhibit the Co and CoP NPs with sufficient interfacial interaction. Further, the existence of Co (111), CoP (112), and CoP (211) phases along with C (120) fringes are confirmed from HRTEM images (Fig. 3d, e).

The selected area electron diffraction (SAED) pattern reveals the

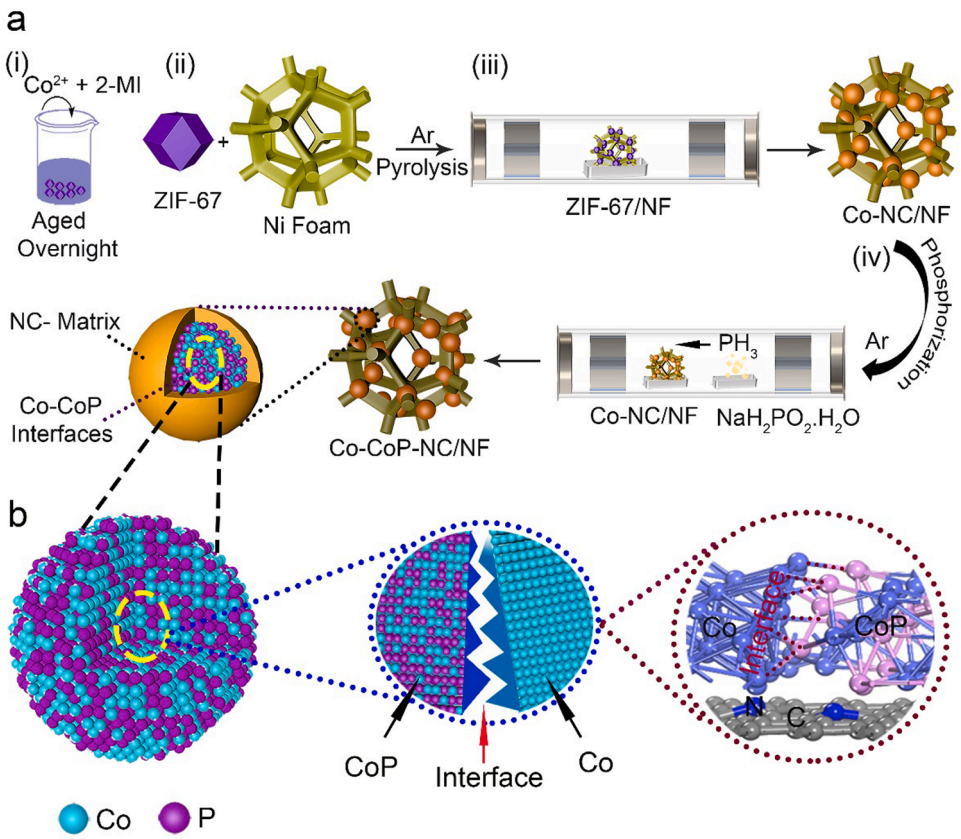

Fig. 1. (a) Schematic diagram expressing the preparation of (i) ZIF-67, (ii) ZIF-67/NF, (iii) Co-NC/NF, (iv) Co-CoP-NC/NF, and (b) the structural illustration of Co-CoP-NC/NF catalyst.

diffraction fringes of C (103) (JCPDS No. 50–0926), CoP (201), (031), (503) (JCPDS No. 29–0497), and Co (200) (JCPDS No. 15–0806) in Fig. 3f and Table S2. Scanning transmission electron microscopic high-angle annular-dark-field (STEM-HAADF) confirms the uniform distribution of Co, P, O, N and C throughout the catalyst (Fig. 3g). Thus, these results confirm the successful preparation of monolithic Co-CoP-NC/NF-2 catalyst.

The composition and chemical state of Co-CoP-NC/NF-2 is studied by XPS analysis. XPS survey spectrum expresses the characteristics peaks for Co 2p, P 2p, O 1 s, N 1 s, and C 1 s at 782.6, 133.3, 531.8, 399.0, and 285.0 eV, respectively (Fig. 4a). The high-resolution XPS spectrum of Co 2p has been deconvoluted into Co peaks at 781.7 corresponding to Co-P [50,51]. The existence of the Co peak (783.5 eV) may be attributed to the surface oxidation of the Co_xP species in the Co-CoP-NC/NF [20,52]. The peak at 778.6 eV expresses the existence of metallic Co^0 [27,44,53], consistent with the PXRD results. The peaks at 786.3 and 803.2 eV correspond to satellite peaks due to spin-orbit splitting [54,55]. The binding energy shift of Co towards higher binding energy in Co-CoP-NC/NF-2 in comparison to Co-NC/NF confirms the electronic transfer from Co metal to more electronegative P. Thus, the effective modulation of the electronic structure of Co metal is dedicated to P-inducing into Co-NC/NF precursor (Fig. 4b). The peaks at 133.8 and 134.1 eV in the high-resolution XPS spectrum of P 2p correspond to the Co-P bond while the peak at 134.7 eV reflects the P-O bond due to unavoidable surface oxidation [20,48,56] (Fig. 4c). The deconvoluted peaks at 531.7 and 533.1 eV in XPS fitting of O 1 s refer to adsorbed H_2O and -OH bond (Fig. 4d). The disappearance of Co-O in Co-CoP-NC/NF-2 in comparison to Co-NC/NF is attributed to P-inducing [20]. Further, the atomic % composition of Co-CoP-NC/NF-2 shows the existence of P (12.38%) in the prepared catalyst (Table S3). The XPS spectrum of C 1 s is deconvoluted into three peaks: 284.8 (C-C), 285.7 (C═N), and 288.6 eV (C═O) [27] (Fig. 4e). The high-resolution XPS profile of N 1 s expresses three peaks at 399.0, 400.8, and 402.0 eV corresponding to pyridinic, pyrrolic, and graphitic N, indicating the successful doping of N into the carbon matrix [57,58] (Fig. 4f). The N-doped graphitic carbon contributes to the incorporation and dispersion of the metallic active sites to improve the stability and catalytic activity of the catalyst [27]. Thus, this analysis confirms the successful inducing of P in the monolithic Co-CoP-NC/NF-2 catalyst.

3.2. Catalytic activity

The temperature dependence of Co-CoP-NC/NF-2 is studied for the temperature range 303–318 K (Fig. 5a). The specific rate of H_2 evolution (r_B) increases from 2500 to 4691 mL $min^{-1}g_{Co}^{-1}$ with the increase in temperature from 303 to 318 K, respectively. The high temperature leads to higher ionic interaction between active sites and the reaction mixture, thus expressing higher catalytic activity. The apparent activation energy (E_a) is calculated as 30.6 kJ mol^{-1} from the slope of the Arrhenius plot (Fig. 5b), using the Arrhenius equation (Eq. (4)).

$$\ln(TOF) = -\frac{E_a}{RT} + \ln A \tag{4}$$

where, TOF = turnover frequency, R = ideal gas constant, T = reaction temperature (K), and A = pre-exponential factor.

The received lower E_a value for Co-CoP-NC/NF-2 is comparable to previously reported noble metal catalysts [59,60]. Thus, the phenomenal lower apparent activation energy (E_a) positions the as-prepared catalyst among the prime noble metal catalysts. Further, the higher turn-over frequency (TOF) and specific rate of hydrogen evolution (r_B) values prove the excellency of Co-CoP-NC/NF compared to previously reported nickel foam-based catalysts [22,61]. In addition, the activation parameters such as $\Delta H^{\#}$ and $\Delta S^{\#}$ (where $\Delta H^{\#}$ and $\Delta S^{\#}$ express the

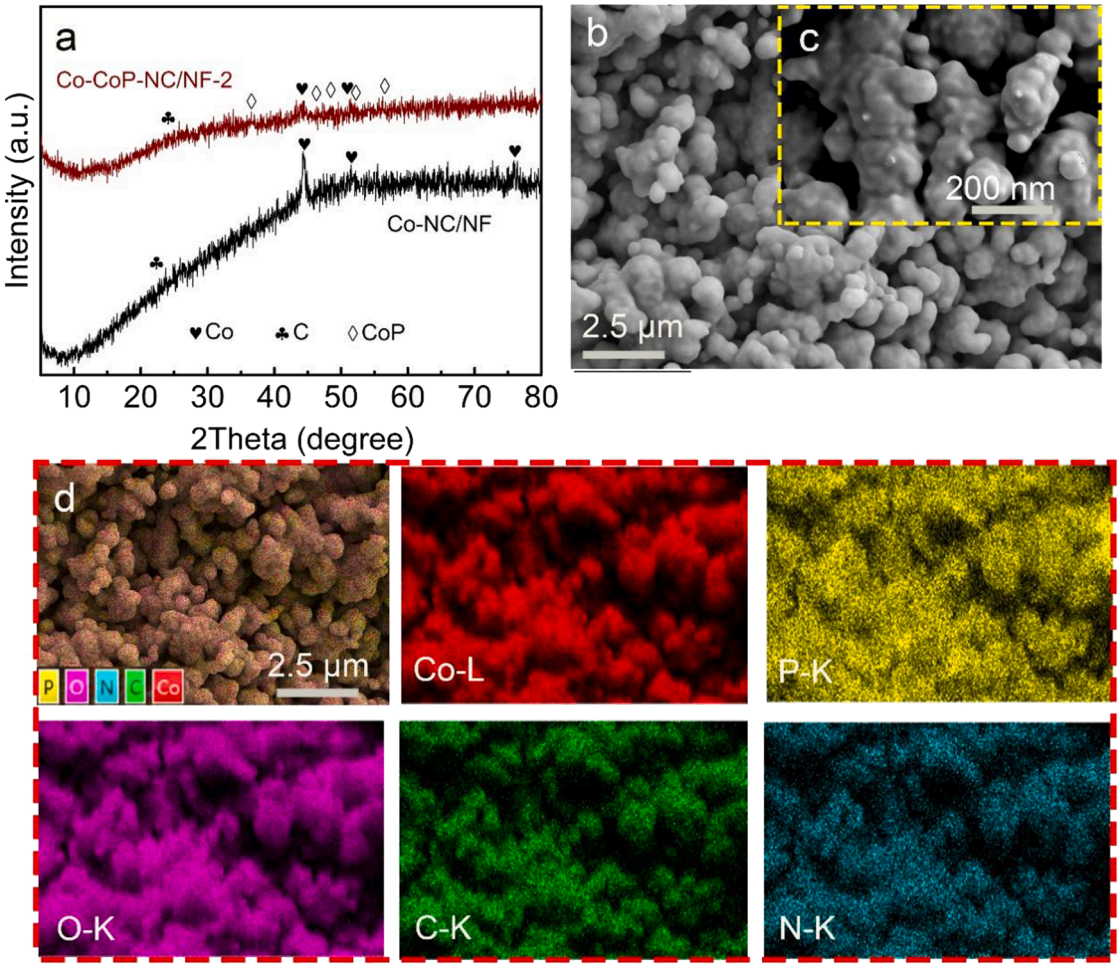

Fig. 2. (a) PXRD pattern of Co-CoP-NC/NF-2 and Co-NC/NF, (b) SEM images low, and (c) high-magnification, and (d) EDS and elemental mapping of Co-CoP-NC/NF-2 catalyst.

energy changes from the initial state to the transition state) are calculated using the Eyring formula [20] (Eq. (5)).

$$\ln (r_B/T) = \ln (k_B/h) + (\Delta S^{\#}/R) - (\Delta H^{\#}/R)\,(1/T) \quad (5)$$

Here, R = the ideal gas constant (8.314 J K^{-1} mol^{-1}), T = the reaction temperature (K), k_B = Boltzmann constant (1.381 × 10^{-23} J K^{-1}), h = Planck's (6.626 × 10^{-34} J s), ΔH^* = activation enthalpy, and ΔS^* = the entropy.

The large positive and negative values of ΔH^* (28.13 k J mol) and ΔS^* (−87.30 J mol^{-1} K^{-1}) imply an associative mechanism at the transition state during the NH_3BH_3 hydrolysis, respectively (Fig. S5b). The extent of the conversion of ammonia borane to hydrogen is studied and the equivalent H_2 per mole of NH_3BH_3 versus time is received for the optimized catalyst (Fig. S5c). Thus, the as-prepared monolithic Co-CoP-NC/NF-2 efficiently generates the equivalent of three moles of hydrogen, consistent with Eq. (1). The reusability test of Co-CoP-NC/NF-2 is performed using a heating treatment. The catalyst expresses 45% retention of catalytic activity after the 5th use in comparison to the 1st use. In contrast, without heating, the catalyst retains only 36% catalytic activity after five uses (Fig. S6). Thus, the heat treatment shows a positive effect on the recyclability of Co-CoP-NC/NF-2. The heating in the air regulates the surface defects and structural properties of Co-CoP-NC/NF-2 [62]. The reduction in catalytic activity after five uses is due to the slight aggregation of Co-CoP NPs, surface leaching, and borate ions adsorption on active sites. Thus, the catalyst maintains its intrinsic properties for up to five uses for NH_3BH_3 hydrolysis. Furthermore, the as-prepared monolithic catalyst is suitable for industrial application due to its facile use and recollection from the reaction mixture. The as-prepared monolithic catalyst Co-CoP-NC/NF-2 is compared with different prepared materials under the same reaction conditions (Fig. 5c). Impressively, the phosphorized catalyst Co-CoP-NC/NF-2 expresses a higher catalytic activity in contrast to Co-NC/NF and other compared materials. The compared materials Co-NC/NF (r_B = 1230 mL $min^{-1}g_{Co}^{-1}$, TOF = 300 h^{-1}) and ZIF-67/NF (r_B = 681 mL $min^{-1}g_{Co}^{-1}$, TOF = 180 h^{-1}) express lower catalytic activities. The catalyst Co-CoP-NC/NF-2 (r_B = 1204 mL $min^{-1}g_{Co}^{-1}$, TOF = 190.08 h^{-1}) and Co-NC/NF (r_B = 0 mL $min^{-1}g_{Co}^{-1}$, TOF = 0 h^{-1}) prepare via in situ strategy express low catalytic activities in comparison to Co-CoP-NC/NF-2 (r_B = 2500 mL $min^{-1}g_{Co}^{-1}$, TOF = 600 h^{-1}). The lower NH_3BH_3 hydrolysis from in situ catalysts is due to the low or negligible loading of active metal on Ni foam. Thus, the manual coated strategy is promising to control the desired loading of active metal on Ni foam [27] (Fig. S7). Pristine Ni foam express NH_3BH_3 hydrolysis (V_{H2} = 130 mL, time = 364 min) with an extremely slow reaction rate. This catalytic activity may be due to the existence of surface oxides on Ni foam. Although after pyrolysis, Ni foam expresses no catalytic activity (r_B = 0 mL $min^{-1}g_{Ni}^{-1}$, TOF = 0 h^{-1}). In contrast, the surface-phosphorized Ni foam is catalytically active with low r_B = 6 mL $min^{-1}g_{Ni}^{-1}$ and TOF = 0.9 h^{-1}. This fact is attributed to the existence of a hexagonal Ni_2P phase (JCPDS No. 03–0953) after the PH_3-phosphorization of Ni foam (Fig. S4b). The lower catalytic activity of powder Co-CoP-NC (r_B = 148 mL $min^{-1}g_{Co}^{-1}$, TOF = 38.52 h^{-1}) proves the advantage of monolithic catalyst Co-CoP-NC/NF-2 over powdery catalysts. PXRD pattern confirms the orthorhombic CoP phases (JCPDS No. 29–0497) in powder

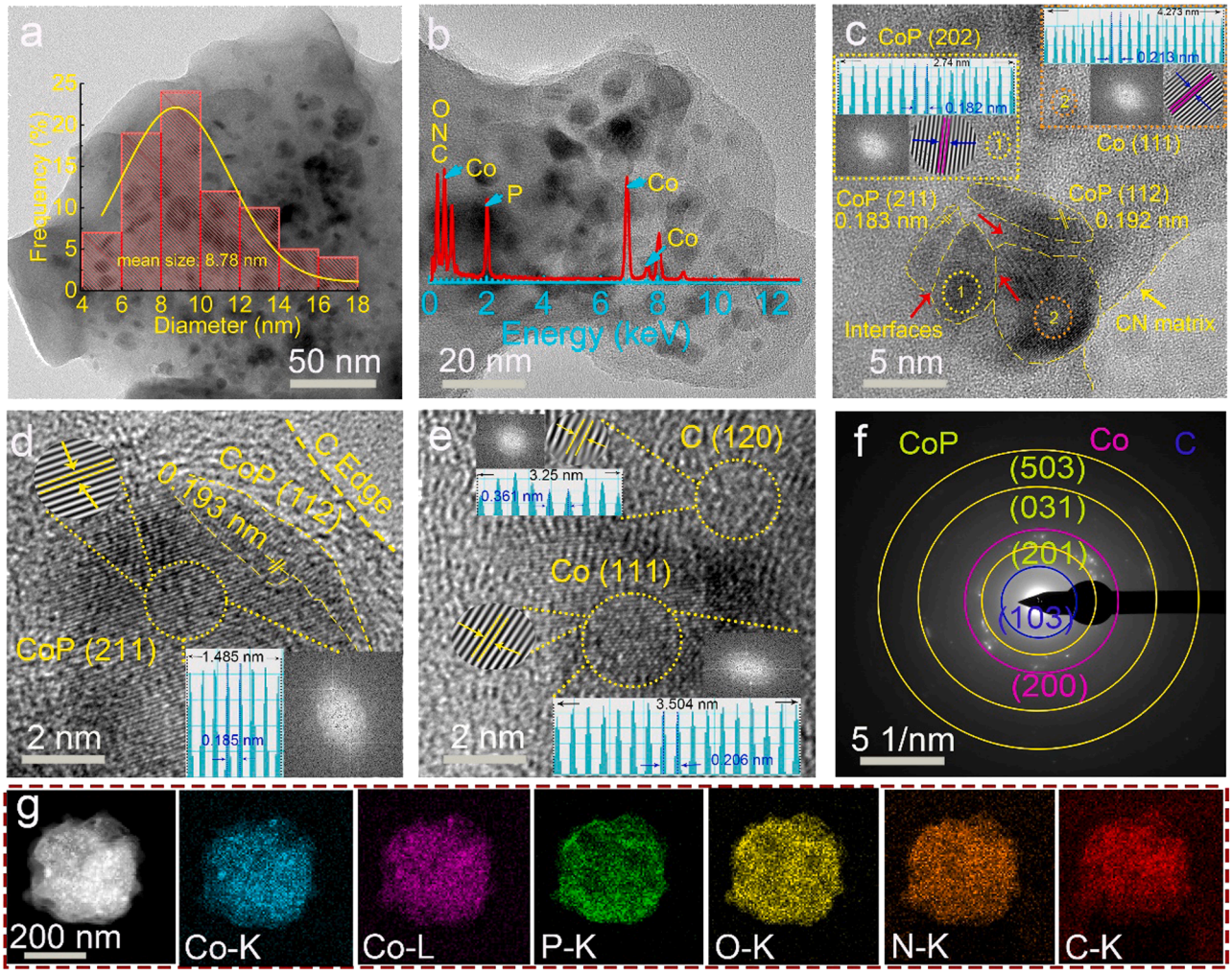

Fig. 3. (a) TEM image with inset histogram of nanoparticle size, (b) TEM image with inset energy dispersive X-ray (EDX spectrum), (c-e) high-resolution TEM images (HRTEM) images (including the corresponding fast Fourier transform (FFT), inverse fast Fourier transform (IFFT) patterns and the atomic intensity profiles), (f) selected area electron diffraction (SAED) pattern, and (g) STEM-HAADF and elemental mapping images of Co-CoP-NC/NF-2.

Co-CoP-NC similar to the monolithic catalyst Co-CoP-NC/NF-2 (Fig. S8). The similar PXRD result proves the successful fabrication of Co-CoP-NC material on Ni foam. This analysis shows the synergistic contribution of Ni foam to the efficient diffusion of reactants (NH_3BH_3 + H_2O) and products (NH_4^+ + BO_2^- + 3 H_2) during the catalytic reaction [24]. Further, the P-inducing into the carbon-nitrogen matrix improves the adsorption of NH_3BH_3 molecules [13]. Thus, it is concluded that the PH_3-phosphorization has induced new active sites (Co and Co-P) and interfacial interaction among the Co-CoP NPs fabricated on Ni foam. Therefore, the phosphorized catalyst Co-CoP-NC/NF-2 is more catalytically active as compared to those without phosphorization. Thus, the comparison results prove the efficiency of the as-prepared monolithic catalyst Co-CoP-NC/NF-2 over other compared materials (Fig. 5d).

3.3. Catalytic kinetics evaluation

The effect of NH_3BH_3 amount on hydrogen evolution for optimized Co-CoP-NC/NF-2 is studied (Fig. 6a). The r_B increases with the increase in the amount of NH_3BH_3. The nearly 14th times increase in r_B values from 393 ($TOF = 102\ h^{-1}$) to 5382 mL min^{-1} g_{Co}^{-1} ($TOF = 1382.4\ h^{-1}$) is observed from 0.58 to 4.6 mmol of NH_3BH_3 amount, respectively (Fig. 6b). The catalytic activity of Co-CoP-NC/NF-2 shows a linear positive relationship versus the amount of NH_3BH_3 [16]. Along with this, the less steep slope of V_{H2} (mL) versus time (min) expresses negligible dependence of H_2 evolution on the amount of NH_3BH_3 [22, 31]. The slope of the logarithmic plot of the H_2 evolution rate relative to the amount of NH_3BH_3 is 1.32 (Fig. 6c). The effect of catalyst amount on hydrogen evolution is studied (Fig. 6d). The NH_3BH_3 and H_2O solution show no hydrogen generation without a catalyst (Fig. S9). The rate of H_2 evolution increases positively with an increase in the amount of Co fabricated on Ni foam from 2.2 to 10 mg. The r_B values are 1304 ($TOF = 72\ h^{-1}$), 1428 ($TOF = 222\ h^{-1}$), 2500 ($TOF = 600\ h^{-1}$), and 3750 ($TOF = 810\ h^{-1}$) mL min^{-1} g_{Co}^{-1} for 2.2 mg, 4.8 mg, 9.2 and 10 mg, respectively. Thus, an increase in the values of r_B and TOF is received from 2.2 to 10 mg due to a reduction in reaction time from 21.137 to 1.595 min for 60 mL of H_2. The fabricated amount of Co (mg) higher than 10 mg reduces the r_B and TOF values due to a large amount of catalyst (w_{Co}, n_{Co}) in the hydrolysis formula (Eqs. (2) and (3)). Thus, an optimum amount of fabricated Co (9.2–10 mg) on Ni foam is suitable to maintain the cost-effectiveness of the catalyst. The slope of the logarithmic plot of TOF relative to the amount of catalyst is 0.97, revealing 1st-order kinetics versus catalyst amount (Fig. 6f). Thus, the catalytic kinetic evaluation reveals that the H_2 generation mainly depends on the structural property of the catalyst instead of the catalyst and NH_3BH_3 amount [63]. The monolithic Co-CoP-NC/NF-2 exhibits efficient hydrogen generation from NH_3BH_3 hydrolysis as compared to other transition metal-based catalysts reported in the literature (Table S4).

Further, the structural characteristics of the catalyst after NH_3BH_3 hydrolysis are studied. The PXRD pattern of the monolithic heat-treated catalyst after one cycle and five cycles without heat treatment show no

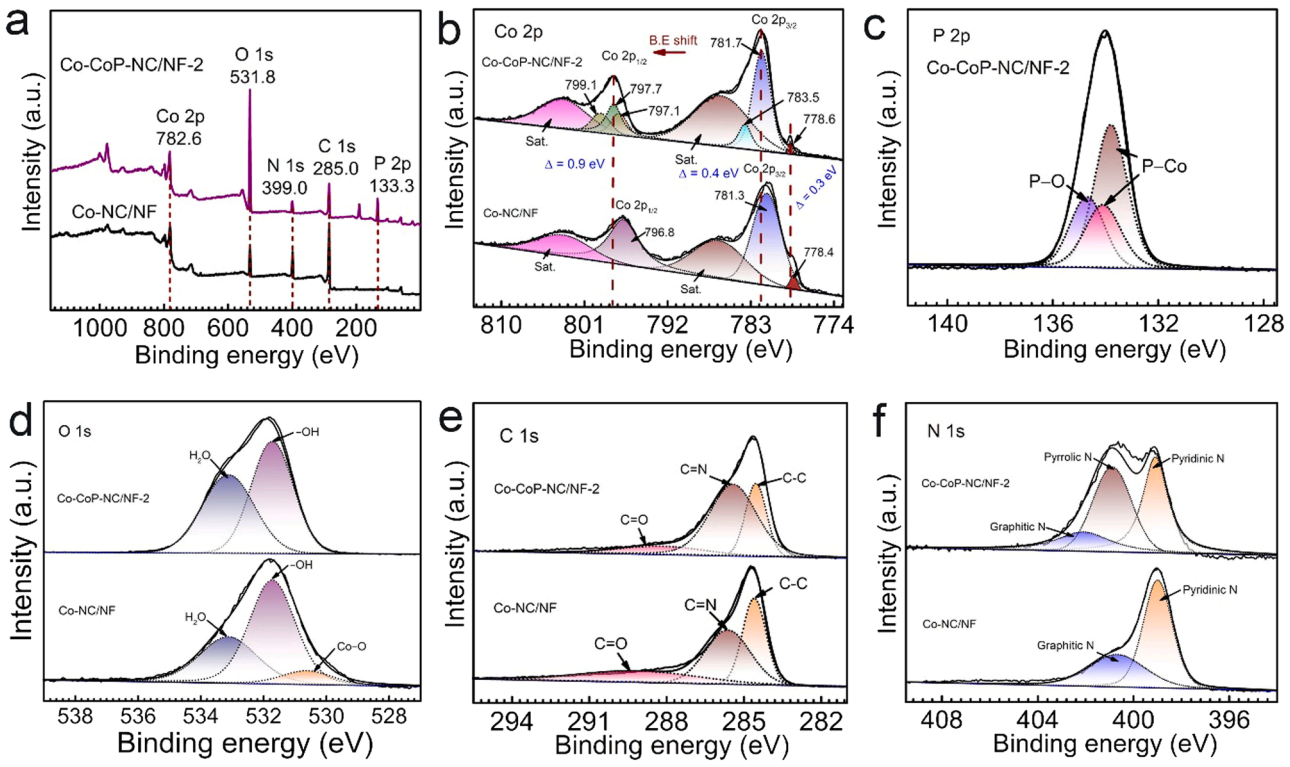

Fig. 4. XPS spectrum of Co-CoP-NC/NF-2: (a) XPS survey spectrum, (b) Co 2p, (c) P 2p, (d) O 1s, (e) C 1s, and (f) N 1s.

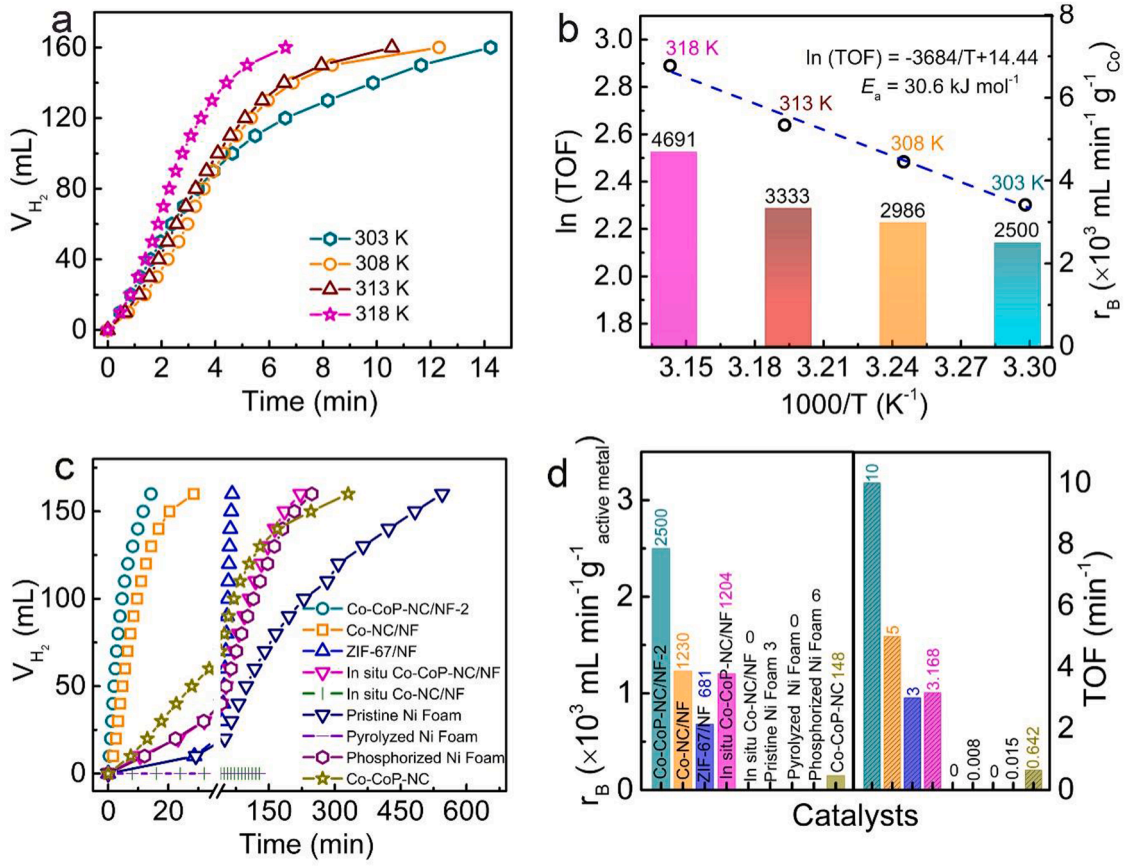

Fig. 5. (a) The effect of temperature on H_2 evolution, (b) the Arrhenius plot and specific rate of H_2 evolution (r_B) at different temperatures, (c) the comparison of hydrogen evolution, and (d) the column plot of comparison for r_B and *TOF* from different materials.

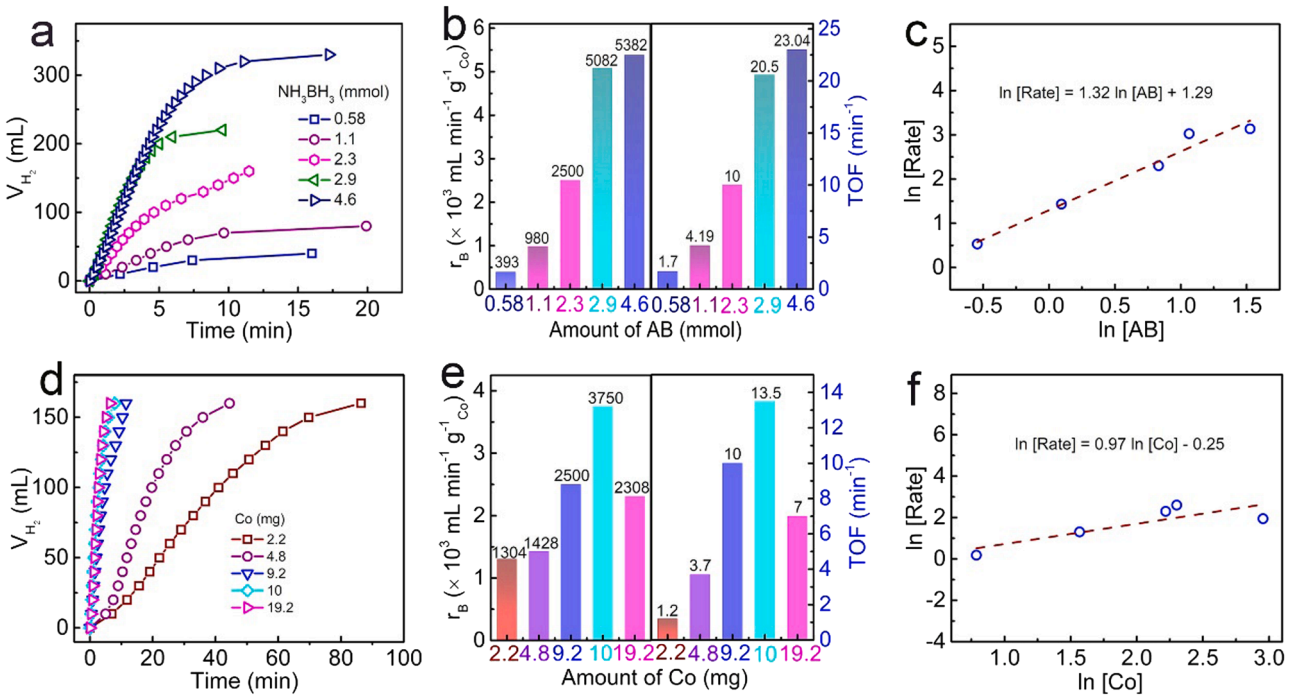

Fig. 6. (a) The plot of hydrogen generation volume (V_{H2}) vs time, (b) the column plot of the specific rate of H_2 evolution (r_B) and turnover frequency (*TOF*) vs the different amounts of NH_3BH_3, (c) the logarithmic plot of turn over frequency (*TOF*) vs the different amount of NH_3BH_3, (d) the plot of hydrogen generation volume (V_{H2}) vs time, (e) the plot of specific rate of H_2 evolution (r_B) and turn over frequency (*TOF*) vs the different amount of catalyst, and (f) the logarithmic plot of turn over frequency (*TOF*) vs the different amount of Co fabricated on Ni foam for Co-CoP-NC/NF-2.

prominent change in phase structure. Although, the phase structure in the catalyst used for five cycles with heat treatment expresses an obvious change, indicating the prominent structure defects (Fig. S10). Thus, the crystal phase structure of Co-CoP-NC/NF-2 expresses stability without heating and shows structural defects on heat treatment after the reusability test. The structural characteristics of powdery Co-CoP-NC catalyst after NH_3BH_3 hydrolysis are studied in comparison to monolithic Co-CoP-NC/NF-2 (Fig. S11). The weakness of the Co (111), and Co (200) phases at 44.2°, 51.5°, and CoP (211) phase at 48.1° positions in the PXRD pattern of powder catalyst express the sufficient leaching of active species (Co-CoP NPs) during the catalytic reaction. The weak diffraction peaks in powdery catalysts Co-CoP-NC express the prominent loss of crystallinity as compared to monolithic catalyst Co-CoP-NC/NF-2. The PXRD pattern of Ni foam after AB hydrolysis exhibits structural stability (Fig. S12). Thus, the as-prepared monolithic catalyst Co-CoP-NC/NF expresses stability after NH_3BH_3 hydrolysis due to its robust structure. TEM images show no prominent change in the structure of the catalyst after catalytic activity except for a minor agglomeration (11.41 nm) of nanoparticles. In addition, the minor agglomeration is dedicated to the inducing of B specie after NH_3BH_3 hydrolysis (Table S3). Thus, the monolithic Co-CoP-NC/NF-2 proves agglomeration resistant due to P-inducing. The high-resolution TEM (HRTEM) image reveals the encapsulation of Co-CoP NPs in carbon rings corresponds to C (120) with lattice fringes of 0.387 nm (Fig. S13). Thus, the heating phenomenon enhances the graphitic carbon encapsulation around the catalytic active sites. Further, this phenomenon avoids the Co-CoP NPs agglomeration during the reusability test [64]. Thus, the heating phenomenon preserves the structural property of Co-CoP-NC/NF-2 for five cycles. The XPS profile comparison of fresh and used catalysts expresses a minor Co 2p shift towards lower binding energy. This shift is attributed to the change in the electronic state of Co due to the heating of the catalyst in the air [62]. XPS spectra of the Co 2p after NH_3BH_3 hydrolysis express the diminishing of the metallic Co^0 peak. The existence of the only Co^{2+} peak shows the conversion of Co^0 into Co^{2+} possibly due to the formation of the Co_xB during the catalytic process. In addition, the presence of the CoO bond in the XPS spectrum of the O 1 s in the used catalyst shows the oxidation of the catalyst during the catalytic process [3,27]. The shift in P 2p after AB hydrolysis corresponds to the slight changes in the states of P species. Thus, the heating process slightly modulates the catalytic activity of active sites. The XPS profile of B 1 s shows a peak at 191.9 eV indicating the existence of B-O-based species in the used catalyst [65–67] (Fig. S14). The reduction in catalytic activity is due to the adsorption of BO_2^- ions on metallic active sites [27]. Thus, an optimum heating phenomenon stipulates the surface defects and intrinsic properties of the catalyst for the reusability test [62,68,69]. Thus, it is evident that the P-inducing in the monolithic catalyst Co-CoP-NC/NF-2 expresses robust structural properties for the retention of catalytic activity during NH_3BH_3 hydrolysis.

3.4. DFT analysis for the mechanism of catalytic reaction

The catalytic mechanism involving NH_3BH_3 hydrolysis on Co-CoP-NC/NF catalyst was elaborated via DFT simulations using the Perdew-Burke-Ernzerhof (PBE) functional (Supporting Information). The atomic structure of simulated catalysts Co (111), CoP (211), Co-CoP, and Co-CoP-NC is shown in Fig. S15. The correlation calculation of adsorption energies of Co, CoP, Co-CoP, and Co-CoP-NC for ammonia borane hydrogen production is studied with a simplified model (Table S5). In the optimum Co-CoP-NC catalyst, Co-activates ammonia borane, and CoP activates water molecules. From a kinetics perspective, the difference of reaction activation barrier (ΔE) for NH_3BH_3 dissociation for different calculated catalyst CoP (0.861 eV), Co (0.666 eV), Co-CoP (0.572 eV), and Co-CoP-NC (0.456 eV) express the lowest ΔE for Co-CoP-NC (Fig. 7a). Similarly, the difference of ΔE for H_2O dissociation for different calculated catalyst CoP (0.679 eV), Co (1.014 eV), Co-CoP (0.587 eV), and Co-CoP-NC (0.302 eV) shows the lowest ΔE for Co-CoP-NC (Fig. 7b). Thus, the theoretical perspective directs the higher affinity of the monolithic catalyst Co-CoP-NC for dissociation of NH_3BH_3 and H_2O in comparison to other simulated catalysts (Co, CoP, Co-CoP). Along with this, the lower adsorption energy of Co-CoP in comparison

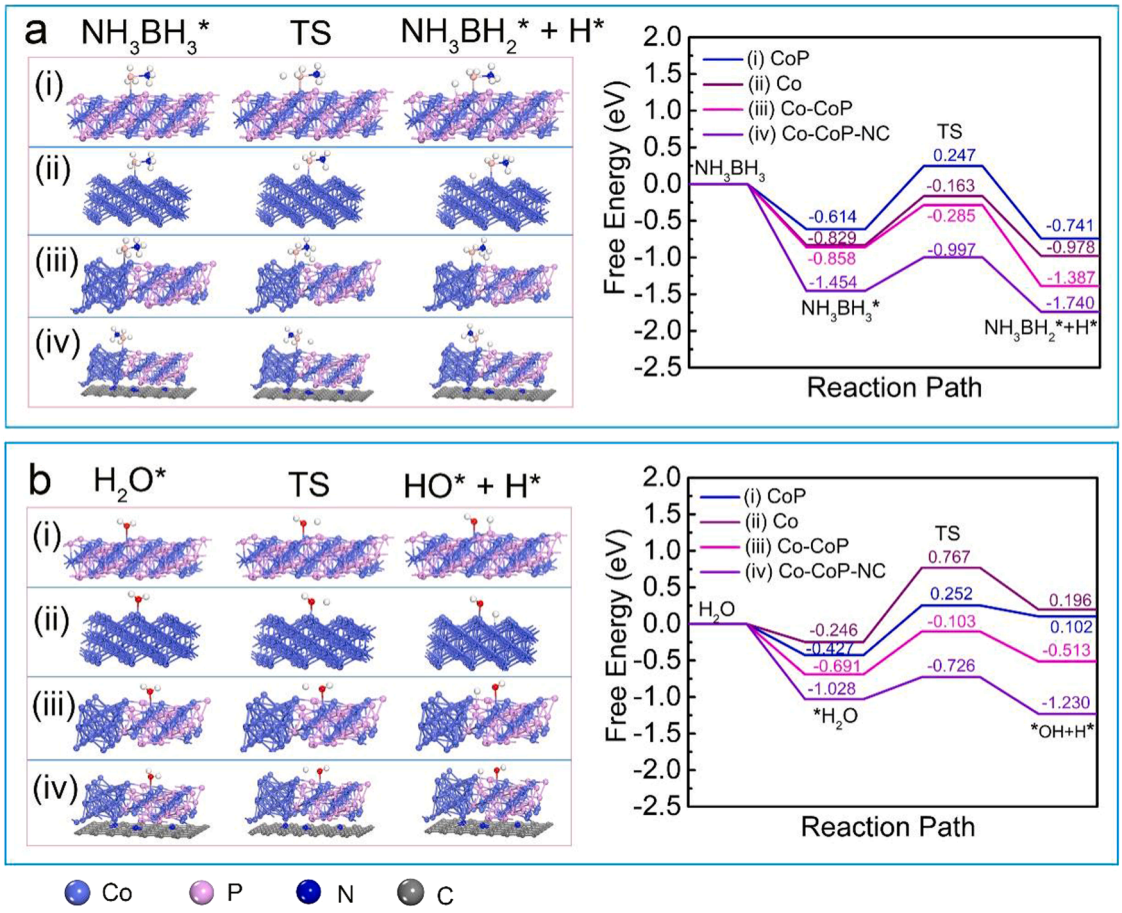

Fig. 7. The energy profile of (a) NH_3BH_3 and (b) H_2O adsorption and dissociation on Co (111), CoP (211), Co-CoP, and Co-CoP-NC along with simulated models expressing the adsorption, activation, and dissociation steps for NH_3BH_3 and H_2O molecules during NH_3BH_3 hydrolysis.

to individual components (Co and CoP) indicates the contribution of the interfacial effect for boosting catalytic activity. Similarly, the lower energy barrier of Co-CoP-NC confirms that the carbon-nitrogen matrix (CN) facilitates the catalytic process by reducing the activation energy. Further, regarding the designation of active sites, ΔE of NH_3BH_3 dissociation on the Co active site (0.666 eV) is lower than that for Co-P (0.861 eV). Similarly, ΔE of H_2O on Co-P (0.679 eV) is lower than Co (1.014 eV). Thus, the P-inducing develops an electron-deficient CoP active site, suitable for the efficient dissociation of the H_2O molecule. Being the rate-determining step of the NH_3BH_3 hydrolysis, possibly the inducing of more electronegative P promotes the activation and dissociation of the H_2O molecule, leading to efficient hydrogen generation [35]. Thus, this analysis confirms the higher affinity of Co and Co-P active sites towards NH_3BH_3 and H_2O molecules, respectively. The monolithic Co-CoP-NC/NF is the optimal catalyst due to the existence of an interfacial active site of Co and Co-P. The construction of interfaces synergistically accelerates electronic transfer, enhances the surface reaction kinetics, and further boosts the catalytic activity [14]. In conclusion, the above-simplified DFT studies strongly confirm the structural favorability and catalytic ability of the monolithic catalyst Co-CoP-NC for the dissociation of NH_3BH_3 and H_2O on their respective active sites (Co and CoP).

From a mechanism perspective, the representation of NH_3BH_3 hydrolysis on the surface of the catalyst is more complex than the DFT simulation, as expressed in Fig. 8a. Generally, the hydrolysis process initiates by the physical adsorption of reactant molecules (NH_3BH_3 and H_2O) on the catalyst surface. Next, the adsorbed molecules are activated to form transition state (TS) species. Lastly, the activated transition state (TS) is dissociated into product species (H_2 and NH_4BO_2) (Fig. 8b). To understand the detailed dissociation and interaction of NH_3BH_3 and H_2O molecules on the surface of optimum catalyst Co-CoP-NC/NF-2, the proposed mechanism follows the given path (Eq. (6)):

$$NH_3BH_3 + [Co]^* \rightarrow NH_3BH_2H\text{-}[Co]^* \quad (6-1)$$

$$H_2O + [Co\text{-}P]^* \rightarrow OHH\text{-}[Co\text{-}P]^* \quad (6-2)$$

$$NH_3BH_2H\text{-}[Co]^* + OHH\text{-}[Co\text{-}P]^* \rightarrow NH_3BH_2\text{-}[Co]^*\text{–}H\text{–}OHH\text{-}[Co\text{-}P]^* \quad (6-3)$$

$$NH_3BH_2\text{-}[Co]^*\text{–}H\text{–}OHH\text{-}[Co\text{-}P]^* + [Co\text{-}P]^* \rightarrow NH_3BH_2\text{-}[Co]^*\text{–}OHH\text{-}[Co\text{-}P]^* + [H]\text{-}[Co]^* \quad (6-4)$$

$$NH_3BH_2\text{-}[Co]^*\text{–}OHH\text{-}[Co\text{-}P]^* \rightarrow NH_3BH_2OH\text{-}[Co]^* + [H]\text{-}[Co\text{-}P]^* \quad (6-5)$$

$$H\text{-}[Co]^* + H\text{-}[Co\text{-}P]^* \rightarrow H_2\uparrow + [Co]^* + [Co\text{-}P]^* \quad (6-6)$$

$$NH_3BH_2OH\text{-}[Co]^* + [Co\text{-}P]^* + H_2O \rightarrow NH_3BH_2OH\text{-}[Co]^*\text{–}OHH\text{-}[Co\text{-}P]^* \quad (6-7)$$

$$NH_3BH_2OH\text{-}[Co]^*\text{–}OHH\text{-}[Co\text{-}P]^* \rightarrow NH_3BHOH\text{-}[Co]^*\text{–}OHH\text{-}[Co\text{-}P]^* + [H]\text{-}[Co]^* \quad (6-8)$$

$$NH_3BHOH\text{-}[Co]^*\text{–}OHH\text{-}[Co\text{-}P]^* \rightarrow NH_3BH(OH)_2\text{-}[Co]^* + H\text{-}[Co\text{-}P]^* \quad (6-9)$$

$$[H]\text{-}[Co]^* + H\text{-}[Co\text{-}P]^* \rightarrow H_2\uparrow + [Co]^* + [Co\text{-}P]^* \quad (6-10)$$

$$NH_3BH(OH)_2\text{-}[Co]^* \rightarrow H_2O + NH_3BHO\text{-}[Co]^* \quad (6-11)$$

$$NH_3BHO\text{-}[Co]^* + [Co\text{-}P]^* + H_2O \rightarrow NH_3BHO\text{-}[Co]^*\text{–}\ OHH\text{-}[Co\text{-}P]^* \quad (6-12)$$

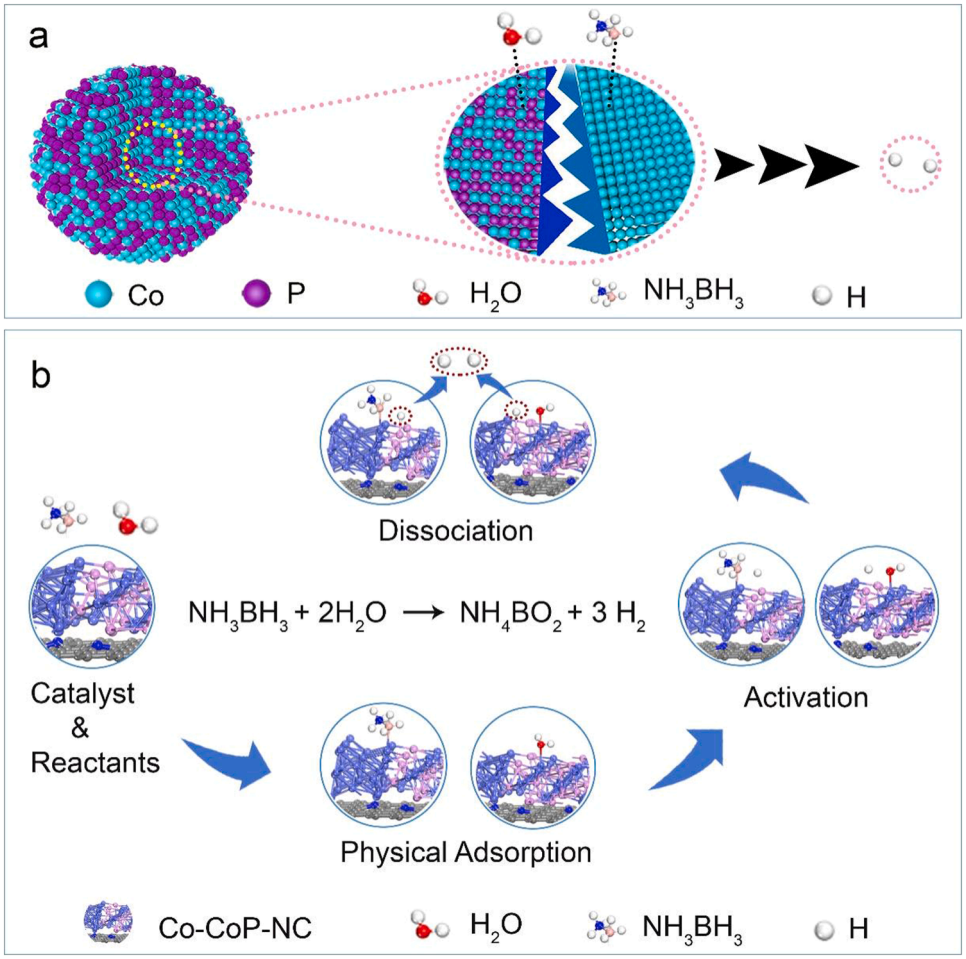

Fig. 8. (a) The representation of NH_3BH_3 hydrolysis on the surface of the catalyst, and (b) the mechanism path involving the liberation of hydrogen from NH_3BH_3.

NH_3BHO-[Co]*–OHH-[Co-P]* → NH_3BO-[Co]*–OHH-[Co-P]* + [Co]*-[H] (6−13)

NH_3BO-[Co]*–OHH-[Co-P]* → NH_3BOOH-[Co]* + H-[Co-P]* (6−14)

[Co]*-[H] + H-[Co-P]* → $H_2\uparrow$ + [Co]* + [Co-P]* (6−15)

NH_3BOOH-[Co]* → $NH_4^+ + BO_2^-$ + [Co]* (6−16)

From the above mechanism, it is proposed that the electron-rich Co-active site activates the B-H bond in the NH_3BH_3 molecule by absorbing the B atom. The O-H bond of the H_2O molecule is activated by the electron-deficient Co-P site absorbing the O atom of H_2O. The catalytic process occurs across the interface of Co and Co-P. Firstly, Co(-Co) atoms adsorb NH_3BH_3 and activate its B-H bond. Then Co(-P) atoms adsorb the H_2O molecule to activate its O-H bond. The activated B-H and O-H bonds of adsorbed NH_3BH_3 and H_2O molecules interact with each other on their respective active sites. This catalytic interaction results in the decomposition of NH_3BH_3 with an intermediate NH_3BH_2-Co* –OHH-[Co-P]* and one H* radical through an oxidation addition. In the next step, the intermediate NH_3BH_2-Co* –OHH-[Co-P]* decomposes into another H* radical through an oxidation addition. Then, the NH_3BH_2OH specie is formed with immediate desorption of H_2 molecules from the catalyst surface through a reduction elimination. Subsequently, Co(-P) atoms activate another H_2O molecule and adsorb with NH_3BH_2OH to form the intermediate NH_3BH_2OH-[Co]* –OHH-[Co-P]* . This process causes the breaking of the second H atom of the NH_3BH_3 molecule. Afterward, the H_2O molecule adsorbed with NH_3BH_2OH decomposes to one H atom and OH bonded to $NH_3BH(OH)_2$. This process results in the second H_2 molecule liberation through the sequence oxidation addition-reduction elimination steps. Due to its instability, $NH_3BH(OH)_2$-[Co]* dissociates immediately into NH_3BHO-[Co]* and H_2O. Finally, the third H_2O molecule is activated on CoP active sites. Meanwhile, adsorbed OHH-CoP* strikes with the B-H bond to release another H atom of AB molecule and results in NH_3BO-[Co]* –OHH-[Co-P]* species. Afterward, the third H_2O molecule dissociates into OH species bonded to NH_3BOOH-[Co]* and one H* radical. This step liberates the third H_2 molecule. NH_3BOOH-[Co]* dissociates into NH_4^+ and BO_2^- and completes the catalytic cycles due to the strong affinity of NH_3 towards H^+ ions [8,14,20]. Thus, monolithic Co-CoP-NC/NF has the advantage of uniform dispersion of Co and CoP NPs into the carbon-nitrogen matrix, and strongly coupled contact between Co and P [35]. These factors collectively lead to efficient catalytic hydrogen generation from the surface of the monolithic catalyst. It is concluded that the bimolecular activation reaction of NH_3BH_3 hydrolysis originates on Co-CoP active sites. Further, the Co-CoP-NC interfaces provide a promising electronic modulated environment for efficient catalytic reaction.

4. Conclusions

In summary, the P-induced monolithic Co-CoP-NC/NF with interfacial effect is synthesized with a PH_3-phosphorization strategy using the novel manually coated precursor. The optimized catalyst Co-CoP-NC/NF-2 express the efficient catalytic activity for ammonia borane hydrolysis with hydrogen evolution (r_B = 2500 mL min^{-1} g_{Co}^{-1}), turnover frequency (TOF = 600 h^{-1}), and apparent activation energy (E_a = 30.6 kJ mol^{-1}). The surface phosphorization enhances the number of active sites and the development of Co-CoP interfaces fabricated on Ni foam. The PH_3-phosphorization results in the P-inducing with sufficient

interfacial interaction between the Co and CoP active sites embedded into the carbon-nitrogen matrix, implying an improvement in the catalytic activity. The as-prepared catalyst expresses the promising *TOF* with the effective activation of NH_3BH_3 molecule on Co-Co and H_2O on Co-P active sites. The DFT results confirm that the Co-CoP-NC catalyst has optimal catalytic activity with the synergistic effect of interfaces toward ammonia borane hydrolysis. Thus, the as-prepared catalyst expresses robust structural properties, and superior catalytic activity compared to other reported nickel foam-based monolithic catalysts for ammonia borane hydrolysis. Therefore, the reported catalyst is positioned among the popular monolithic catalysts in the literature. This novel rational design strategy for monolithic catalysts will find great potential in those fields of heterogeneous catalysis and the sustainable energy industry.

CRediT authorship contribution statement

Sehrish Mehdi: Investigation, Visualization, Writing – original draft, Writing – review & editing, Formal analysis. **Yanyan Liu:** Investigation, Visualization, Writing – review & editing, Formal analysis. **Huijuan Wei:** Investigation, Visualization, Formal analysis, the supporting of contribution. **Huanhuan Zhang**: Formal analysis, the supporting of contribution. **Ruofan Shen**: Formal analysis, the supporting of contribution. **Shuyan Guan**: Formal analysis, the supporting of contribution. **Xianli Wu**: Formal analysis, the supporting of contribution. **Tao Liu**: Formal analysis, the supporting of contribution. **Hao Wen**: Formal analysis, the supporting of contribution. **Zhikun Peng**: Formal analysis, the supporting of contribution. **Chengming Wang:** Investigation, Visualization, Writing – review & editing, Formal analysis. **Zhongyi Liu**: Investigation, Visualization, Formal analysis, the supporting of contribution. **Huaqiang Cao**: Visualization, Formal analysis, the Supporting of contribution. **Baojun Li:** Visualization, Formal analysis, Supervision, Conceptualization, The lead of contribution.

Declaration of Competing Interest

The authors declare that they have no known competing financial interests or personal relationships that could have appeared to influence the work reported in this paper.

Data availability

No data was used for the research described in the article.

Acknowledgments

Financial support from the National Natural Science Foundation of China (Nos. 22075254, 31901272, 22279117, and 22279118) is acknowledged. All authors thank the inspiration of China–Pakistan Economic Corridor.

Appendix A. Supplementary material

Supplementary data associated with this article can be found in the online version at doi:10.1016/j.apcatb.2022.122317.

References

[1] W.W. Zhan, Q.L. Zhu, Q. Xu, Dehydrogenation of ammonia borane by metal nanoparticle catalysts, ACS Catal. 6 (2016) 6892–6905.
[2] J. Guo, B. Wang, D. Yang, Z. Wan, P. Yan, J. Tian, T.T. Isimjan, X. Yang, Rugae-like Ni_2P-CoP nanoarrays as a bi-functional catalyst for hydrogen generation: $NaBH_4$ hydrolysis and water reduction, Appl. Catal. B Environ. 265 (2020), 118584.
[3] H. Zhang, Y. Fan, B. Liu, Y. Liu, S. Ashraf, X. Wu, G. Han, J. Gao, B. Li, Birdcage-type CoOx-carbon catalyst derived from metal–organic frameworks for enhanced hydrogen generation, ACS Sustain. Chem. Eng. 7 (2019) 9782–9792.
[4] N. Patel, A. Kale, A. Miotello, Improved dehydrogenation of ammonia borane over Co-P-B coating on Ni: a single catalyst for both hydrolysis and thermolysis, Appl. Catal. B Environ. 111 (2012) 178–184.
[5] K. Feng, J. Zhong, B. Zhao, H. Zhang, L. Xu, X. Sun, S.T. Lee, $Cu_xCo_{1-x}O$ nanoparticles on graphene oxide as a synergistic catalyst for high-efficiency hydrolysis of ammonia–borane, Angew. Chem. Int. Ed. 55 (2016) 11950–11954.
[6] J. Zhang, W. Chen, H. Ge, C. Chen, W. Yan, Z. Gao, J. Gan, B. Zhang, X. Duan, Y. Qin, Synergistic effects in atomic-layer-deposited PtCox/CNTs catalysts enhancing hydrolytic dehydrogenation of ammonia borane, Appl. Catal. B Environ. 235 (2018) 256–263.
[7] Q. Yao, Y. Ding, Z.H. Lu, Noble-metal-free nanocatalysts for hydrogen generation from boron-and nitrogen-based hydrides, Inorg. Chem. Front. 7 (2020) 3837–3874.
[8] S. Guan, L. An, S. Ashraf, L. Zhang, B. Liu, Y. Fan, B. Li, Oxygen vacancy excites Co_3O_4 nanocrystals embedded into carbon nitride for accelerated hydrogen generation, Appl. Catal. B Environ. 269 (2020), 118775.
[9] M.A. Khalily, H. Eren, S. Akbayrak, H.H. Susapto, N. Biyikli, S. Özkar, M.O. Guler, Facile synthesis of three-dimensional Pt-TiO_2 nano-networks: a highly active catalyst for the hydrolytic dehydrogenation of ammonia–borane, Angew. Chem. Int. Ed. 55 (2016) 12257–12261.
[10] Z. Li, Q. Pei, Y. Yu, Z. Jing, J. Wang, T. He, Syntheses of Pt-Ni hollow nanoalloy for hydrogen generation from catalytic hydrolysis of ammonia borane, ChemCatChem 12 (2020) 4257–4261.
[11] Z. Wei, Y. Liu, Z. Peng, H. Song, Z. Liu, B. Liu, B. Li, B. Yang, S. Lu, Cobalt-Ruthenium nanoalloys parceled in porous nitrogen-doped graphene as highly efficient difunctional catalysts for hydrogen evolution reaction and hydrolysis of ammonia borane, ACS Sustain. Chem. Eng. 7 (2019) 7014–7023.
[12] C. Wang, D. Astruc, Recent developments of nanocatalyzed liquid-phase hydrogen generation, Chem. Soc. Rev. 50 (2021) 3437–3484.
[13] Y. Lin, L. Yang, H. Jiang, Y. Zhang, D. Cao, C. Wu, G. Zhang, J. Jiang, L. Song, Boosted reactivity of ammonia borane dehydrogenation over Ni/Ni_2P heterostructure, J. Phys. Chem. Lett. 10 (2019) 1048–1054.
[14] H. Zhang, Y. Liu, H. Wei, C. Wang, T. Liu, X. Wu, S. Ashraf, S. Mehdi, S. Guan, Y. Fan, Atomic-bridge structure in B-Co-P dual-active sites on boron nitride nanosheets for catalytic hydrogen generation, Appl. Catal. B Environ. 314 (2022), 121495.
[15] C. Cui, Y. Liu, S. Mehdi, H. Wen, B. Zhou, J. Li, B. Li, Enhancing effect of Fe-doping on the activity of nano Ni catalyst towards hydrogen evolution from NH_3BH_3, Appl. Catal. B Environ. 265 (2020), 118612.
[16] X. Huang, Y. Liu, H. Wen, R. Shen, S. Mehdi, X. Wu, E. Liang, X. Guo, B. Li, Ensemble-boosting effect of Ru-Cu alloy on catalytic activity towards hydrogen evolution in ammonia borane hydrolysis, Appl. Catal. B Environ. 287 (2021), 119960.
[17] B.C. Filiz, A.K. Figen, S. Pişkin, The remarkable role of metal promoters on the catalytic activity of Co-Cu based nanoparticles for boosting hydrogen evolution: ammonia borane hydrolysis, Appl. Catal. B Environ. 238 (2018) 365–380.
[18] Y. Yuan, X.Y. Chen, X. Zhang, Z.M. Wang, R.B. Yu, A MOF-derived CuCo(O) @carbon-nitrogen framework as an efficient synergistic catalyst for the hydrolysis of ammonia borane, Inorg. Chem. Front. 7 (2020) 2043–2049.
[19] C. Yu, F. Xu, L. Luo, H.S. Abbo, S.J. Titinchi, P.K. Shen, P. Tsiakaras, S. Yin, Bimetallic Ni-Co phosphide nanosheets self-supported on nickel foam as high-performance electrocatalyst for hydrogen evolution reaction, Electrochim. Acta 317 (2019) 191–198.
[20] H. Zhang, K. Zhang, S. Ashraf, Y. Fan, S. Guan, X. Wu, Y. Liu, B. Liu, B. Li, Polar O–Co–P surface for bimolecular activation in catalytic hydrogen generation, Energy Environ. Mater. (2022), https://doi.org/10.1002/eem2.12273.
[21] Z. Chen, X. Zeng, X. Li, Z. Lv, J. Li, Y. Zhang, Strong metal phosphide–phosphate support interaction for enhanced non-noble metal catalysis, Adv. Mater. 34 (2022), 2106724.
[22] J. Yang, Q. Yuan, Y. Liu, X. Huang, Y. Qiao, J. Lu, C. Song, Low-cost ternary Ni–Fe–P catalysts supported on Ni foam for hydrolysis of ammonia borane, Inorg. Chem. Front. 6 (2019) 1189–1194.
[23] C. Tang, L. Xie, K. Wang, G. Du, A.M. Asiri, Y. Luo, X. Sun, A Ni2P nanosheet array integrated on 3D Ni foam: an efficient, robust and reusable monolithic catalyst for the hydrolytic dehydrogenation of ammonia borane toward on-demand hydrogen generation, J. Mater. Chem. A 4 (2016) 12407–12410.
[24] M. Asim, S. Zhang, Y. Wang, B. Maryam, M. Sajid, C. Shi, L. Pan, X. Zhang, J.J. Zou, Self-supporting NiCoP for hydrogen generation via hydrolysis of ammonia borane, Fuel 318 (2022), 123544.
[25] C. Tang, F.L. Qu, A.M. Asiri, Y.L. Luo, X.P. Sun, CoP nanoarray: a robust non-noble-metal hydrogen-generating catalyst toward effective hydrolysis of ammonia borane, Inorg. Chem. Front. 4 (2017) 659–662.
[26] L. Xie, K. Wang, G. Du, A.M. Asiri, X. Sun, Self-standing cobalt oxide nanosheet array: an monolithic catalyst for effective hydrolysis of $NaBH_4$ in alkaline media, Int. J. Hydrog. Energy 42 (2017) 30639–30645.
[27] S. Mehdi, Y. Liu, H. Wei, H. Wen, R. Shen, Z. Peng, H. Zhang, X. Wu, C. Wang, S. Guan, T. Liu, B. Li, Co-based nanoparticles fabricated on Ni foams for efficient hydrogen generation from ammonia borane, ACS Appl. Nano Mater. 5 (2022) 5064–5074.
[28] C. Wang, J. Zhao, X. Du, S. Sun, X. Yu, X. Zhang, Z. Lu, L. Li, X. Yang, Hydrogen production from ammonia borane hydrolysis catalyzed by non-noble metal-based materials: a review, J. Mater. Sci. 56 (2021) 2856–2878.
[29] H. Sun, J. Meng, L. Jiao, F. Cheng, J. Chen, A review of transition-metal boride/phosphide-based materials for catalytic hydrogen generation from hydrolysis of boron-hydrides, Inorg. Chem. Front. 5 (2018) 760–772.
[30] X. Zhang, Y. Zhao, X. Jia, Y. Zhao, L. Shang, Q. Wang, G.I.N. Waterhouse, L.Z. Wu, C.H. Tung, T. Zhang, Silica-protected ultrathin Ni_3FeN nanocatalyst for the efficient hydrolytic dehydrogenation of NH_3BH_3, Adv. Energy Mater. 8 (2018), 1702780.

[31] C.C. Hou, Q. Li, C.J. Wang, C.Y. Peng, Q.Q. Chen, H.F. Ye, W.F. Fu, C.M. Che, N. López, Y. Chen, Ternary Ni–Co–P nanoparticles as noble-metal-free catalysts to boost the hydrolytic dehydrogenation of ammonia-borane, Energy Environ. Sci. 10 (2017) 1770–1776.
[32] Y. Shi, M. Li, Y. Yu, B. Zhang, Recent advances in nanostructured transition metal phosphides: synthesis and energy-related applications, Energy Environ. Sci. 13 (2020) 4564–4582.
[33] Y. Wang, G. Shen, Y. Zhang, L. Pan, X. Zhang, J.J. Zou, Visible-light-induced unbalanced charge on NiCoP/TiO_2 sensitized system for rapid H_2 generation from hydrolysis of ammonia borane, Appl. Catal. B Environ. 260 (2020), 118183.
[34] Y. Chen, K. Feng, G. Yuan, Z. Kang, J. Zhong, Highly efficient CoNiP nanoboxes on graphene oxide for the hydrolysis of ammonia borane, Chem. Eng. J. 428 (2022), 131219.
[35] C. Wang, Z. Wang, H. Wang, Y. Chi, M. Wang, D. Cheng, J. Zhang, C. Wu, Z. Zhao, Noble-metal-free Co@Co_2P/N-doped carbon nanotube polyhedron as an efficient catalyst for hydrogen generation from ammonia borane, Int. J. Hydrog. Energy 46 (2021) 9030–9039.
[36] L. Yu, J. Zhang, Y. Dang, J. He, Z. Tobin, P. Kerns, Y. Dou, Y. Jiang, Y. He, S.L. Suib, In situ growth of Ni_2P–Cu_3P bimetallic phosphide with bicontinuous structure on self-supported NiCuC substrate as an efficient hydrogen evolution reaction electrocatalyst, ACS Catal. 9 (2019) 6919–6928.
[37] K. Eom, K. Cho, H. Kwon, Hydrogen generation from hydrolysis of NH_3BH_3 by an electroplated Co–P catalyst, Int. J. Hydrog. Energy 35 (2010) 181–186.
[38] L. Cui, Y. Xu, L. Niu, W. Yang, J. Liu, Monolithically integrated CoP nanowire array: an on/off switch for effective on-demand hydrogen generation via hydrolysis of $NaBH_4$ and NH_3BH_3, Nano Res. 10 (2017) 595–604.
[39] B.N. Kinsiz, B. Coşkuner Filiz, S. Kılıç Depren, A. Kantürk Figen, Nano-casting procedure for catalytic cobalt oxide bead preparation from calcium-alginate capsules: activity in ammonia borane hydrolysis reaction, Appl. Mater. Today 22 (2021), 100952.
[40] J. Yang, F. Cheng, J. Liang, J. Chen, Hydrogen generation by hydrolysis of ammonia borane with a nanoporous cobalt–tungsten–boron–phosphorus catalyst supported on Ni foam, Int. J. Hydrog. Energy 36 (2011) 1411–1417.
[41] L. Huang, R. Yao, X. Wang, S. Sun, X. Zhu, X. Liu, M.G. Kim, J. Lian, F. Liu, Y. Li, H. Zong, S. Han, X. Ding, In situ phosphating of Zn-doped bimetallic skeletons as a versatile electrocatalyst for water splitting, Energy Environ. Sci. 15 (2022) 2425–2434.
[42] F.W. Ming, H.F. Liang, H.H. Shi, X. Xu, G. Mei, Z.C. Wang, MOF-derived Co-doped nickel selenide/C electrocatalysts supported on Ni foam for overall water splitting, J. Mater. Chem. A 4 (2016) 15148–15155.
[43] Y. Zheng, L. Zhang, H. Huang, F. Wang, L. Yin, H. Jiang, D. Wang, J. Yang, G. Zuo, ZIF-67-derived Co, Ni and S co-doped N-enriched porous carbon polyhedron as an efficient electrocatalyst for oxygen evolution reaction (OER), Int. J. Hydrog. Energy 44 (2019) 27465–27471.
[44] G. Yang, S. Guan, S. Mehdi, Y. Fan, B. Liu, B. Li, Co-CoOx supported onto TiO_2 coated with carbon as a catalyst for efficient and stable hydrogen generation from ammonia borane, Green Energy Environ. 6 (2021) 236–243.
[45] W. Sang, C. Wang, X. Zhang, X. Yu, C. Yu, J. Zhao, X. Wang, X. Yang, L. Li, Dendritic $Co_{0.52}Cu_{0.48}$ and $Ni_{0.19}Cu_{0.81}$ alloys as hydrogen generation catalysts via hydrolysis of ammonia borane, Int. J. Hydrog. Energy 42 (2017) 30691–30703.
[46] X. Fan, R. Sun, Y. Zhu, S. Zhang, L. Gou, L. Lu, D. Li, Controllable 3D porous Ni current collector coupled with surface phosphorization enhances Na storage of Ni_3S_2 nanosheet arrays, Small 18 (2022), 2106161.
[47] J. Qin, S. Wang, X. Wang, Visible-light reduction CO_2 with dodecahedral zeolitic imidazolate framework ZIF-67 as an efficient co-catalyst, Appl. Catal. B Environ. 209 (2017) 476–482.
[48] H. Liu, Y. Liu, S. Mehdi, X. Wu, T. Liu, B. Zhou, P. Zhang, J. Jiang, B. Li, Surface phosphorus-induced CoO coupling to monolithic carbon for efficient air electrode of quasi-solid-state Zn–air batteries, Adv. Sci. 8 (2021), 2101314.
[49] J. Liu, Y. Gao, X. Tang, K. Zhan, B. Zhao, B.Y. Xia, Y. Yan, Metal–organic framework-derived hierarchical ultrathin CoP nanosheets for overall water splitting, J. Mater. Chem. A 8 (2020) 19254–19261.
[50] A. Li, L. Zhang, F. Wang, L. Zhang, L. Li, H. Chen, Z. Wei, Rational design of porous Ni-Co-Fe ternary metal phosphides nanobricks as bifunctional electrocatalysts for efficient overall water splitting, Appl. Catal. B Environ. 310 (2022), 121353.
[51] T. Zhang, Y. Wang, J. Yuan, K. Fang, A.J. Wang, Heterostructured CoP·CoMoP nanocages as advanced electrocatalysts for efficient hydrogen evolution over a wide pH range, J. Colloid Interface Sci. 615 (2022) 465–474.
[52] I.K. Mishra, H. Zhou, J. Sun, F. Qin, K. Dahal, J. Bao, S. Chen, Z. Ren, Hierarchical CoP/Ni_5P_4/CoP microsheet arrays as a robust pH-universal electrocatalyst for efficient hydrogen generation, Energy Environ. Sci. 11 (2018) 2246–2252.
[53] Y. Pan, K. Sun, S. Liu, X. Cao, K. Wu, W.-C. Cheong, Z. Chen, Y. Wang, Y. Li, Y. Liu, D. Wang, Q. Peng, C. Chen, Y. Li, Core–shell ZIF-8@ZIF-67-derived CoP nanoparticle-embedded N-doped carbon nanotube hollow polyhedron for efficient overall water splitting, J. Am. Chem. Soc. 140 (2018) 2610–2618.
[54] H. Liu, M. Jin, D. Zhan, J. Wang, X. Cai, Y. Qiu, L. Lai, Stacking faults triggered strain engineering of ZIF-67 derived Ni-Co bimetal phosphide for enhanced overall water splitting, Appl. Catal. B Environ. 272 (2020), 118951.
[55] P. Zhang, Y. Liu, T. Liang, E.H. Ang, X. Zhang, F. Ma, Z. Dai, Nitrogen-doped carbon wrapped Co-Mo_2C dual Mott–Schottky nanosheets with large porosity for efficient water electrolysis, Appl. Catal. B Environ. 284 (2021), 119738.
[56] X. Wu, S. Chen, Y. Feng, Q. Yuan, J. Gao, Y. Chen, Y. Huang, Y.B. He, W. Gan, Microwave-assisted synthesis of carbon nanotubes threaded core-shell CoPx/Co-Nx-C@CNT and its performance as an efficient bifunctional oxygen catalyst for the rechargeable zinc-air battery, Mater. Today Phys. 9 (2019), 100132.
[57] W. Li, Y. Chen, B. Yu, Y. Hu, X. Wang, D. Yang, 3D hollow Co–Fe–P nanoframes immobilized on N,P-doped CNT as an efficient electrocatalyst for overall water splitting, Nanoscale 11 (2019) 17031–17040.
[58] W. Li, B. Yu, Y. Hu, X. Wang, D. Yang, Y. Chen, Core–shell structure of $NiSe_2$ nanoparticles@nitrogen-doped graphene for hydrogen evolution reaction in both acidic and alkaline media, ACS Sustain. Chem. Eng. 7 (2019) 4351–4359.
[59] G. Chen, S. Desinan, R. Rosei, F. Rosei, D. Ma, Synthesis of Ni–Ru alloy nanoparticles and their high catalytic activity in dehydrogenation of ammonia borane, Chem. Eur. J. 18 (2012) 7925–7930.
[60] N. Mohajeri, A.T. Raissi, O. Adebiyi, Hydrolytic cleavage of ammonia-borane complex for hydrogen production, J. Power Sources 167 (2007) 482–485.
[61] K. Eom, M. Kim, R. Kim, D. Nam, H. Kwon, Characterization of hydrogen generation for fuel cells via borane hydrolysis using an electroless-deposited Co-P/Ni foam catalyst, J. Power Sources 195 (2010) 2830–2834.
[62] S. Guan, L. Zhang, H. Zhang, Y. Guo, B. Liu, H. Wen, Y. Fan, B. Li, Defect-rich Co−CoOx-graphene nanocatalysts for efficient hydrogen production from ammonia borane, Chem. Asian J. 15 (2020) 3087–3095.
[63] S. Guan, Y. Liu, H. Zhang, H. Wei, T. Liu, X. Wu, H. Wen, R. Shen, S. Mehdi, X. Ge, C. Wang, B. Liu, E. Liang, Y. Fan, B. Li, Atomic interface-exciting catalysis on cobalt nitride-oxide for accelerating hydrogen generation, Small 18 (2022), 2107417.
[64] T. Chen, R. Zhang, B. Ye, Q. Yang, H. Xu, L. Zheng, L. Wang, Ce-doped CoP nanoparticles embedded in carbon nanotubes as an efficient and durable catalyst for hydrogen evolution, Nanotechnology 31 (2020), 125402.
[65] D. Lim, G. Özkan, G. Özkan, Ni–B and Zr–Ni–B in-situ catalytic performance for hydrogen generation from sodium borohydride, ammonia borane and their mixtures, Int. J. Hydrog. Energy 47 (2022) 3396–3408.
[66] Q. Guo, S. Li, J. Li, Y. Hu, Y. Li, Effect of SiO_2 on the CO selective methanation over SiO_2/Ni-ZrO_2 catalysts, ChemCatChem 14 (2022), 202101281.
[67] M. Paladini, G.M. Arzac, V. Godinho, M.C.J. De Haro, A. Fernandez, Supported Co catalysts prepared as thin films by magnetron sputtering for sodium borohydride and ammonia borane hydrolysis, Appl. Catal. B Environ. 158 (2014) 400–409.
[68] L. Xu, S. Xiong, S. Zhong, S. Bai, Y. Jiao, J. Chen, Metallic cobalt and molybdenum oxides encapsulated in B, N-doped carbon nanocomposite catalyzed hydrogen evolution from ammonia borane hydrolysis, Vacuum 174 (2020), 109213.
[69] W. Feng, L. Yang, N. Cao, C. Du, H. Dai, W. Luo, G. Cheng, In situ facile synthesis of bimetallic CoNi catalyst supported on graphene for hydrolytic dehydrogenation of amine borane, Int. J. Hydrog. Energy 39 (2014) 3371–3380.